


C₆₀ adsorption on a dodecagonal oxide quasicrystalE. M. Zollner,¹ S. Schenk,¹ S. Förster,^{1,*} and W. Widdra^{1,2}¹*Institute of Physics, Martin-Luther-Universität Halle-Wittenberg, D-06099 Halle, Germany*²*Max-Planck-Institut für Mikrostrukturphysik, Weinberg 2, D-06120 Halle, Germany* (Received 30 August 2019; revised manuscript received 24 October 2019; published 14 November 2019)

Quasicrystalline surfaces are potential templates for highly ordered but aperiodic molecular self-assemblies. Here, we report on the adsorption of C₆₀ molecules on a two-dimensional oxide quasicrystal (OQC) and its σ -phase approximant at room temperature and 150 K. The molecular films have been characterized by means of scanning tunneling microscopy and low-energy electron diffraction. A weak interaction of the molecules with the dodecagonal oxide template is found, resulting in a low desorption temperature of 510 K. For low temperatures specific adsorption sites within the tiling of the OQC and the σ -phase approximant have been identified as preferred nucleation sites. The narrow spacing between these sites introduces repulsive interaction between C₆₀ molecules and restricts the epitaxial growth to small patches. At room temperature, C₆₀ nucleates in hcp islands of almost arbitrary rotational orientation on the OQC. A slight orientational preference for hexagonal islands with a 15° rotation against the OQC tiling is discussed as a consequence of the preferential adsorption on the quadratic tiles.

DOI: [10.1103/PhysRevB.100.205414](https://doi.org/10.1103/PhysRevB.100.205414)**I. INTRODUCTION**

The aperiodic long-range order of quasicrystals resembles an extraordinary way of arranging atoms in solid material. Soon after their discovery [1] the question was raised regarding how quasicrystalline ordering would affect the physical properties of a given material. To tackle that question numerous attempts have been made to imprint the quasicrystalline structure by using quasicrystals as templates for thin-film growth [2]. This idea was first successfully applied to inorganic materials like Pb, Cu, and Bi [3–5] and was later extended to molecular overlayers [6,7] and a combination of both [8,9]. Organic materials are promising due to an enhanced structural flexibility which might enable the directed self-assembly of quasiperiodic layers beyond monolayer thicknesses [6,7,10–15]. They are furthermore appealing due to the possibilities of functionalizing molecules to vary their physicochemical properties. The prototypical molecule in adsorption studies on quasicrystals is C₆₀. In the first studies the inert C₆₀ molecules served as a marker for preferred adsorption sites on an icosahedral surface [10]. Since then, the adsorption conditions have been optimized to achieve the growth of continuous films of quasicrystalline order [11–14]. More recently, C₆₀ molecules were found to spontaneously form small patches of a quasicrystalline triangle-square tiling on a hexagonal Pt₃Ti(111) surface [15].

Here, we report adsorption studies on a two-dimensional oxide quasicrystal (OQC). In contrast to the quasicrystalline systems used for adsorption studies so far, this two-dimensional OQC exhibits dodecagonal symmetry. It is derived from an ultrathin BaTiO₃ film on a Pt(111) substrate [16]. A similar structure was also observed in the

SrTiO₃/Pt(111) system [17]. In both systems atomically resolved scanning tunneling microscopy (STM) images showed that the subgrid of the Ti atoms forms a tiling of equilateral triangles, squares, and rhombs of a common edge length of 6.85 Å [16,18]. The tiling statistics agree perfectly with that of an ideal dodecagonal Niizeki-Gähler tiling (NGT) [19–21]. Besides these dodecagonal quasicrystals approximant structures have also been reported for both systems [17,18], which are periodic structures with a complex unit cell that is also present as an element in the quasicrystal. The adsorption studies reported here were conducted using C₆₀ molecules on the BaTiO₃-derived OQC and the σ -phase approximant. The tilings of both structures are sketched in Fig. 1. In contrast to the complex triangle-square-rhomb tiling of the OQC [Fig. 1(a)], the σ -phase approximant [Fig. 1(b)] is a periodic triangle-square tiling. The shaded area in the lower left of both patterns indicates the largest square-triangle patch that is common to both tilings. In the real system, Ti atoms are found at the tiling vertices. The characteristic edge length of about 7 Å does not provide a suitable grid for decoration of all vertices by C₆₀ molecules with their van der Waals (vdW) diameter of 10 Å. However, both tilings offer a variety of distances between equivalent adsorption sites, which are indicated in Fig. 1(b). The vdW diameter of C₆₀ roughly matches the distances between the centers of two neighboring squares of 9.4 Å or two triangles attached to a square of 10.8 Å.

II. EXPERIMENTAL DETAILS

The experiments were performed in standard ultrahigh-vacuum (UHV) systems operating at a base pressure of 10^{−10} mbar. The substrate preparation, BaTiO₃ deposition, and room temperature C₆₀ adsorption experiments were performed in a multifacility chamber (Multiprobe, Omicron). The low-temperature C₆₀ adsorption studies were conducted

*stefan.foerster@physik.uni-halle.de

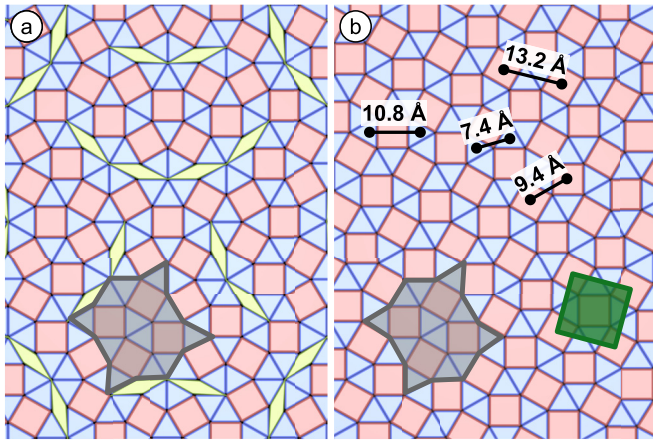


FIG. 1. Schematic tilings of (a) the OQC and (b) the σ -phase approximant. The tiling vertices are formed from Ti atoms in the real system. The largest common tiling patch is shaded in gray. Additionally, the unit cell of the σ -phase approximant is marked green in (b). Various distances between possible adsorption sites are given.

by directly dosing molecules onto the cooled sample inside a variable-temperature STM (VT-SPM, Omicron). The STM was cooled to 150 K by using liquid nitrogen.

The Pt(111) single crystal (Mateck) was cleaned by cycles of Ar⁺ ion sputtering, UHV flashing at 1270 K, and annealing at 900 K in 10^{-6} mbar of O₂ [22].

To fabricate the OQC template, ultrathin BaTiO₃ films were prepared by molecular beam epitaxy on Pt(111) substrates. BaO and Ti were evaporated in an atmosphere of 10^{-6} mbar of O₂ by electron beam evaporation (EFM3, Focus). Ti was supplied by a metal rod, and BaO was supplied by heating a stoichiometric BaTiO₃ ceramic fixed in a Ta crucible. The deposition was monitored using a quartz-crystal microbalance. After subsequent deposition of 2 Å of BaO and 2 Å of TiO_x the ultrathin oxide film was fully oxidized in 10^{-5} mbar O₂ at 920 K for 15 min. The OQC template was prepared by annealing the ultrathin BaTiO₃ film for 5 min at 1120 K in UHV. To prepare the σ -phase approximant this final UHV annealing was performed at 1220 K for 5 min. Temperatures were monitored using a pyrometer (Cyclops 50, Minolta/Land, working at a wavelength of 520 nm) at an emissivity of 0.1. The long-range order of the template was checked by low-energy electron diffraction (LEED) prior to the adsorption experiments. Additionally, x-ray photoelectron spectroscopy was used to confirm the composition and cleanliness. C₆₀ molecules (IoLiTec Nanomaterials, purity of 99.99%) were evaporated from a home-built Knudsen cell at a temperature of 607 K. Prior to deposition the molecules were kept at 570 K in UHV for degassing. The STM images were processed using GWYDDION [23]. To analyze the next-neighbor distances and angular distributions the software package *Mathematica* (Wolfram Research) was used.

III. RESULTS

A. C₆₀ adsorption on the OQC at room temperature

Upon room temperature deposition, C₆₀ molecules are found in two configurations on the OQC-covered Pt(111)

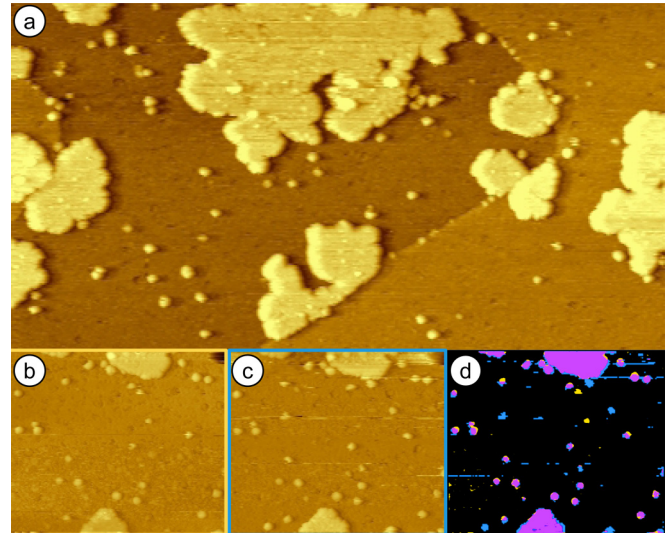


FIG. 2. (a) Large-scale STM image of 0.3 ML C₆₀ adsorbed on the BaTiO₃-derived OQC at room temperature. (b) and (c) Two consecutive STM images on a smaller scale and (d) their difference image show that small C₆₀ clusters are able to hop between defect sites. (a) $500 \times 185 \text{ nm}^2$, (b)–(d) $220 \times 185 \text{ nm}^2$, (a)–(c) $\Delta z = 21 \text{ \AA}$, 0.8 nA, 2.0 V.

surface, which are small C₆₀ clusters and C₆₀ islands of different sizes. Figure 2(a) shows a typical large-scale STM image obtained for a C₆₀ coverage of 0.3 ML. The islands are flat with a height of 8 Å as determined from line profiles at different sample biases. They nucleate predominantly at step edges. The shape of the islands is irregular and does not allow us to conclude on the molecular packing structure. The free OQC in between the C₆₀ islands is decorated with molecular clusters. The different sizes of the clusters indicate that they are formed from more than a single C₆₀ molecule. The cluster height is similar to that of the islands. In contrast to the completely immobilized islands, some clusters are found to move at room temperature. This can be seen from subsequently recorded STM images shown in Figs. 2(b) and 2(c). The two images cover a time span of 10 min. To illustrate the motion of the C₆₀ clusters, the image contrast has been turned to yellow for Fig. 2(b) and blue for Fig. 2(c), and the images were summed. In the sum image in Fig. 2(d), C₆₀ clusters colored magenta did not move from one frame to the other. In contrast, the yellow and blue clusters changed place between the two measurements. Figure 2(d) shows that most of the clusters remain at fixed positions. Most likely, they are pinned to defects in the template.

Upon increasing the coverage to a full monolayer, the growth of the second layer starts long before the first layer is closed. The large-area STM image in Fig. 3 shows that 19% of the OQC area remains uncovered, whereas 14% of the area is already covered by second-layer islands. In the close-up STM image in Fig. 3(b) the molecular packing of the first and second layers is resolved. In both cases the C₆₀ molecules are in a hcp arrangement. However, the orientation of both layers is different, as highlighted by the red and blue lines following the densely packed rows of molecules. Some of the second-layer islands [marked by M in Fig. 3(a)] exhibit

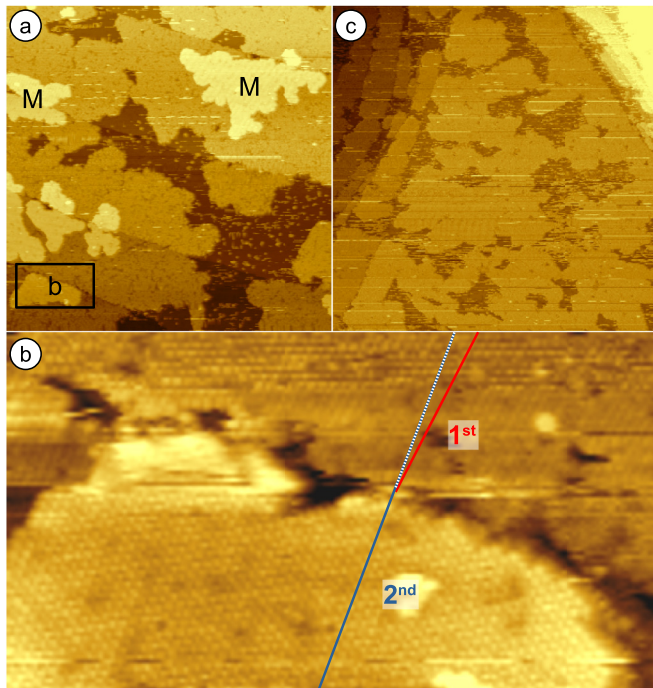


FIG. 3. C₆₀ molecules on the OQC template at a coverage of 1 ML upon (a) and (b) room temperature deposition and (c) annealing at 470 K. The second-layer C₆₀ islands marked by **M** in (a) show a stripelike moiré pattern of different periodicity. (b) Close-up of (a) showing the hcp ordering of C₆₀ in the first- and second-layer islands. (a) 300 × 300 nm², Δz = 15 Å, (b) 63 × 35 nm², (c) 380 × 380 nm², Δz = 47 Å, (a)–(c) 0.8 nA, −1.5 V.

stripelike height modulations of varying periodicity. Most likely, these are moiré patterns resulting from different relative orientations of the C₆₀ islands with respect to the substrate. Annealing the monolayer coverage to temperatures of 470 K does not alter the overall appearance of the first layer of C₆₀ in the STM image, as shown in Fig. 3(c). Still, individual patches of C₆₀ are seen, which are separated by the free OQC area. However, upon annealing at 470 K the second-layer islands have disappeared. Either the molecules of the second layer desorb, or they are incorporated into first-layer patches.

The long-range order of the C₆₀ molecules was investigated using LEED. Figure 4 shows typical LEED patterns of submonolayer to monolayer coverages obtained at 10, 20, and 30 eV kinetic energy. The 12 sharp spots of the OQC template are clearly visible at all energies. In addition, at 10 eV two rings are observed: one at an inverse length of 0.73 Å^{−1} and the second at 1.23 Å^{−1}. At higher kinetic energies two more rings are seen at 1.46 and 1.96 Å^{−1}. Referring to the inner ring, we determine a scaling of the ring dimensions of 1:1.7:2:2.7, which corresponds to the scaling of the lowest index lattice planes in a hexagonal lattice, as illustrated in Fig. 4(d) with ratios of 1:√3:2:√7. Thus, the integral LEED measurement confirms the hcp ordering of C₆₀ molecules in various orientations. From LEED a next-neighbor distance of (9.9 ± 0.1) Å is determined. Looking more carefully at the inner ring at 0.73 Å^{−1}, an anisotropic intensity distribution can be seen. Figure 4(e) shows the superposition of circular

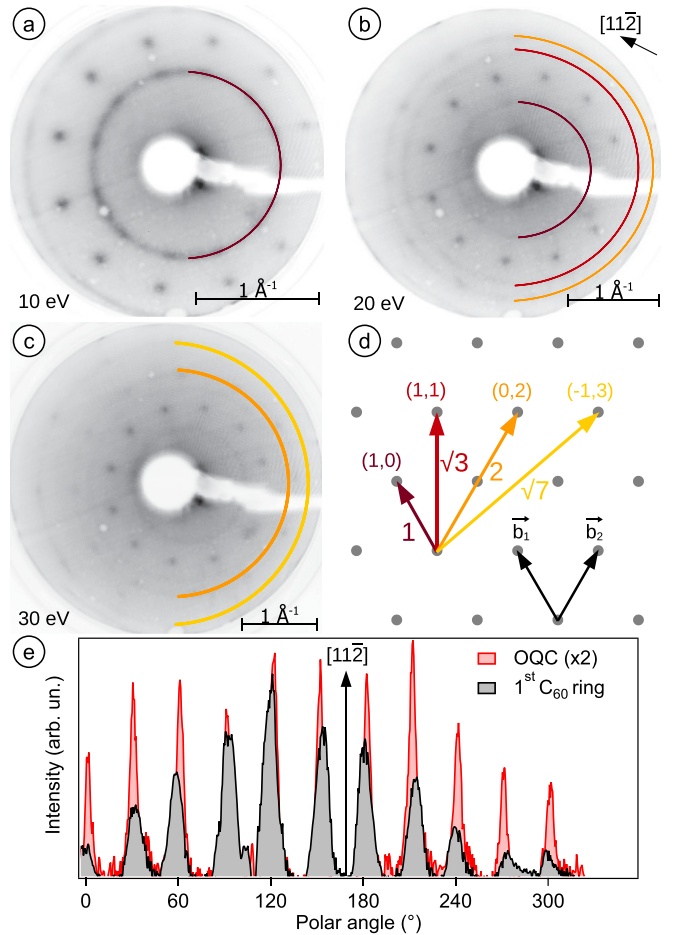


FIG. 4. (a)–(c) LEED pattern of 1 ML C₆₀ on the OQC at room temperature. The half circles mark different rings originating from C₆₀ packing. (d) Schematics showing the scaling of diffraction spots for a hexagonal lattice in reciprocal space. The same scaling is found for the rings in (a)–(c). (e) Circular line profiles along the C₆₀ ring at 0.73 Å^{−1} and the OQC spots.

line profiles of the C₆₀-related ring at 0.73 Å^{−1} (taken at 10 eV) and the intense OQC spots at 1.03 Å^{−1} (taken at 20 eV). After baseline subtraction for the C₆₀ ring, a clear match of the intensity increase with the OQC spots positions is found. This indicates a preferred alignment of hexagonal C₆₀ patches at 15° rotation against the Pt(111) substrate (along [112]) and thus against the edges of the OQC tiling.

Using *in situ* LEED measurements, the desorption temperature of C₆₀ is determined. Figure 5 shows a sequence of LEED images taken at 510 K. At this temperature the C₆₀-related ring at 0.73 Å^{−1} vanishes with time. After 180 s the OQC diffraction pattern appears with a strongly increased intensity due to a complete desorption of C₆₀. Subsequent STM measurements (not shown) confirm the complete desorption of C₆₀.

B. C₆₀ adsorption onto the OQC at 150 K

Upon *in situ* deposition of 0.4-ML C₆₀ onto the OQC template at 150 K, a high density of small C₆₀ clusters of different sizes is observed, as shown in Fig. 6(a). Besides

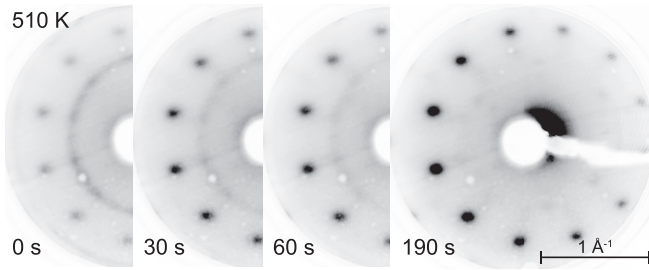


FIG. 5. Temporal evolution of the LEED pattern of the C_{60} covered OQC template during annealing at 510 K. At this temperature the C_{60} desorption occurs.

small clusters individual molecules are also observed. The suppressed C_{60} diffusion at 150 K results in a high nucleation density in the first monolayer as well as in the second layer even on the smallest clusters. The arrangement of C_{60} molecules within the clusters is not restricted to hexagonal packing. In Figs. 6(b)–6(i) various arrangements are shown enlarged. Besides combinations of triangular C_{60} arrangements [Fig. 6(b)], full or incomplete squares have been found [Figs. 6(c) and 6(d)]. Moreover, combinations of triangles and squares are found which resemble motifs of the OQC tiling: a simple arrangement of just one triangle and one square [Fig. 6(e)], two triangles and one square [Fig. 6(f)], and the more complex combination of three triangles and two squares, as shown in Fig. 6(g). Besides triangles and squares, less compact formations like five- and six-membered rings are also formed [Figs. 6(h) and 6(i)]. Note that for all these C_{60} arrangements a next-neighbor distance of about 10 Å must be assumed, according to the room temperature experiments, which does not match the original scaling of tiles in the OQC.

The distribution of C_{60} molecules was further investigated by statistical means. Therefore, the exact coordinates of all molecules were extracted, and the derived point mesh was analyzed with respect to next-neighbor distances and angles. This allows for an unbiased automated search for geometric units formed from neighboring molecules. In the analyzed data we find 472 triangles, 33 complete squares, and 23 isosceles triangles with one right angle, which resemble incomplete squares. Taking the sum of the latter two, the fraction of local quadratic motifs formed from C_{60} molecules amounts to 12%. In the ideal Niizeki-Gähler tiling 24% of all tiles are squares. The orientation of the edges of the equilateral triangles is plotted in Fig. 6(j). It shows three broad maxima centered at 0° , 60° , and 120° , respectively. In addition, we have an increased number of edges pointing to 30° , 90° , and 150° . The distribution can be fitted using two sets of three Gaussian peaks separated by multiples of 60° that are displaced by 30° . This indicates a clear preference for an alignment of equilateral triangles in registry with the OQC template.

C. C_{60} adsorption on the σ -phase approximant at 150 K

For comparison with a less complex template, 0.4 ML of C_{60} were deposited at 150 K on the quadratic grid of the σ -phase approximant [18]. As already seen for the low-temperature deposition of C_{60} onto the OQC, a high density

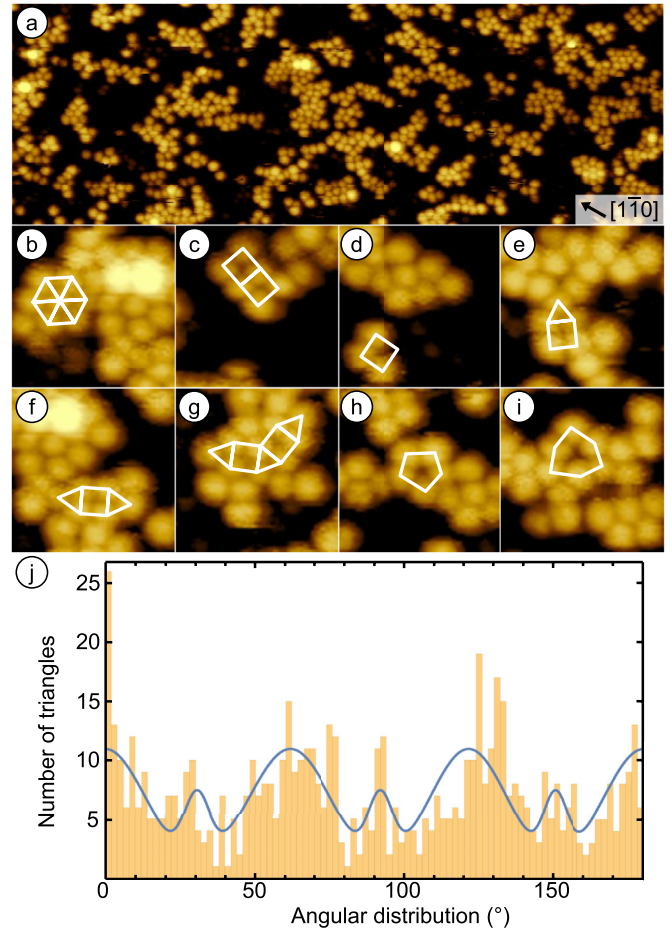


FIG. 6. (a) Large-scale STM image of 0.4 ML of C_{60} molecules on the OQC deposited and measured at 150 K. (b)–(i) Close-up images of the different combinations of triangles and squares found in (a). (j) Orientational distribution of equilateral triangles on the OQC template. (a) $82 \times 28 \text{ nm}^2$, $\Delta z = 10 \text{ \AA}$, 66 pA, 2.5 V, (b)–(i) $7.5 \times 7.5 \text{ nm}^2$.

of smallest clusters and individual molecules are observed by STM. The large-scale image in Fig. 7(a) shows that typically, two to four molecules are lined up in rows with a clear preference of the horizontal and vertical directions of the image (defined as 0° and 90°). Already, this leads to the impression that the quadratic template strongly directs the assembly of C_{60} on the surface. The alignment of the molecules with respect to the σ -phase unit cell becomes possible due to the stripelike moiré structure formed by the σ phase on the Pt(111) substrate [18]. This moiré becomes visible in the background of Fig. 7(a) by adjusting the contrast (not shown here). The moiré-induced stripes appear under a rotation of 15° against the vertical direction of the image. The σ -phase unit cell is rotated by 30° against the stripes of the moiré [18]. Consequently, the alignment of the molecular rows with respect to the σ -phase unit vectors cannot unambiguously be determined here; it is either 45° or 75° .

The radial distribution function of C_{60} pairs on the σ -phase approximant is presented in Fig. 7(b). For smaller distances, three distinct maxima are found, whereas for larger distances the distribution becomes unspecific. The three maxima range

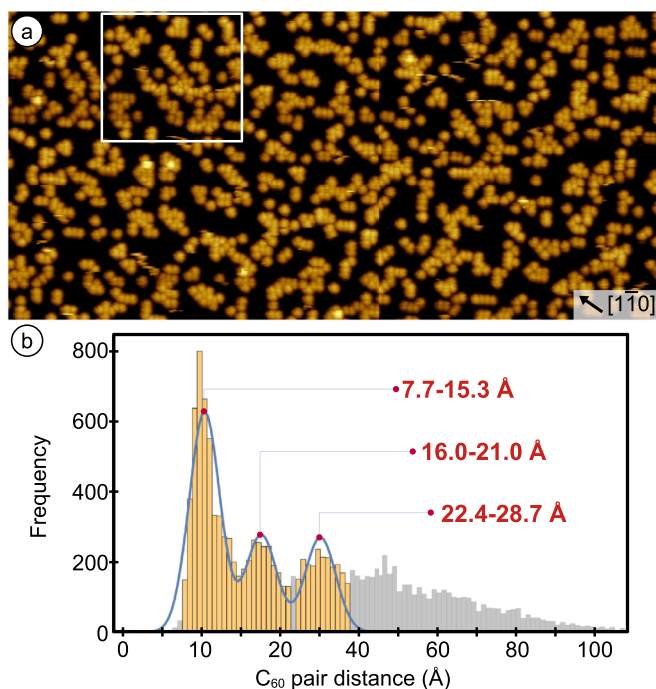


FIG. 7. (a) Large-scale STM image of 0.4 ML of C₆₀ molecules adsorbed on the σ -phase approximant at 150 K. The area inside the white square is analyzed in detail in Fig. 8. (b) Histogram of the radial distribution function of intermolecular distances in C₆₀ pairs in gray. The three maxima highlighted by yellow bars are further analyzed in Fig. 8. (a) $117 \times 55 \text{ nm}^2$, $\Delta z = 10 \text{ \AA}$, 80 pA, 2.6 V.

from 7.7 to 15.3, 16.0 to 21.0, and 22.4 to 28.7 \AA . The angular distribution of C₆₀ pairs with a distance between 7.7 and 15.3 \AA is plotted in Fig. 8(a). There, two sharp maxima at 0° and 90° and two broader maxima at about 40° and 130° are observed. Within this distance range, the shortest distances are found at 0° and 90° . The STM data set has been calibrated by centering this shortest intermolecular distance to 9.9 \AA , which is the C₆₀ spacing determined from LEED at room temperature before. Under a rotation of roughly 45° the average distance of C₆₀ pairs is enlarged to roughly 13 \AA . The angular distribution of C₆₀ pairs with distances between 16 and 20.4 \AA in Fig. 8(c) reveals six maxima. Two are again centered at 0° and 90° . The others are shifted by $\pm 30^\circ$ against the latter ones. For C₆₀ pairs with distances between 23.0 and 26.8 \AA , eight maxima are clearly distinguishable in the angular distribution shown in Fig. 8(e). These distances are again found under 0° and 90° angles. In addition, they occur under $\pm 20^\circ$ rotations around the previous ones. Furthermore, clear maxima are found at $\pm 45^\circ$. The derived distances and angles agree well with a decoration of centers of the square tiles which will be discussed in detail later.

By increasing the C₆₀ coverage to 0.6 ML, the lateral size of the patches grows. In addition, adsorption in the second layer occurs as shown in Fig. 9(a). Here, about 87% of the molecules are adsorbed in the first layer, while 13% are already located in the second layer. The plot of the radial pair distribution shown in Fig. 9(b) is dominated by only one maximum centered at 10 \AA . Despite the visual impression

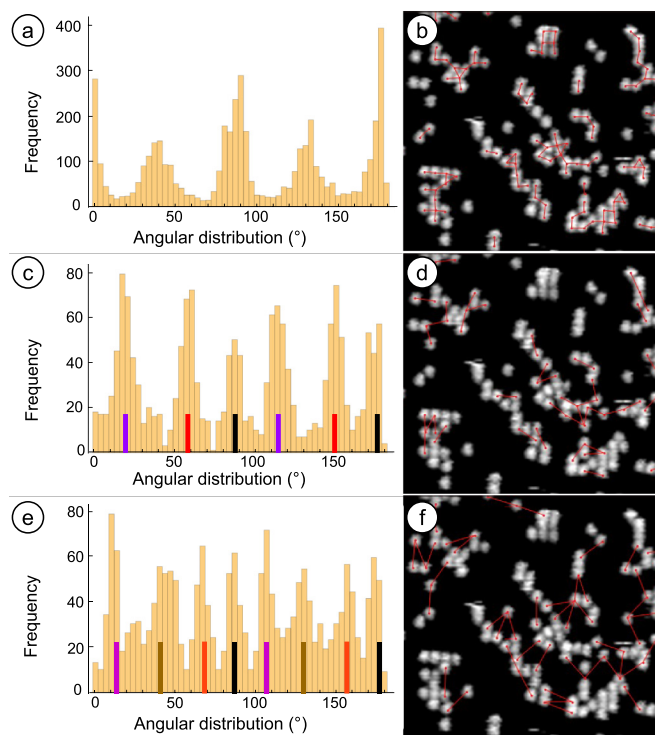


FIG. 8. Analysis of the alignment of neighboring C₆₀ molecules for different intermolecular distances: (a) and (b) 8–12 \AA , (c) and (d) 16–20 \AA , and (e) and (f) 25–30 \AA . Angles are given with respect to the horizontal direction. The colored bars correspond to the C₆₀ pair distances discussed in Fig. 10. (b), (d), and (f) Close-up of the region inside the white frame in Fig. 7(a), $30 \times 27 \text{ nm}^2$, 80 pA, 2.6 V.

of the formation of enlarged extended patches, the lack of additional peaks in the radial distribution function indicates a missing long-range coherence in the C₆₀ ordering. The angular distribution of C₆₀ pairs for distances from 7.7 to 15.3 \AA is plotted in Fig. 9(c). It is quite similar to that of the lower coverage shown in Fig. 8(a), indicating that the nearest-neighbor arrangement is not changed.

IV. DISCUSSION

The low-temperature adsorption of C₆₀ on the σ -phase approximant at 0.4-ML coverage is characterized by the emergence of three classes of preferred intermolecular distances as read from the radial pair-distribution function presented in Fig. 7(b): 7.7 to 15.5, 16.0 to 21.0, and 22.4 to 28.7 \AA . Within these classes, the C₆₀ pairs are oriented in very distinct directions, as seen in Fig. 8. The densest mesh of equivalent adsorption sites in the σ -phase roughly matching the vdW radius of C₆₀ is provided by the centers of the squares. In Fig. 10 the seven shortest pair distances provided by these adsorption sites are drawn. The corresponding values of distances and orientations are listed in Table I. Here, the experimentally observed distances and angles are also included. For comparison, we assume an orientation of the shortest C₆₀ pairs of 45° with respect to the σ -phase unit vectors. The first maximum of the radial distribution function of C₆₀ pairs in Fig. 7(b) consists of two different distances. The shortest

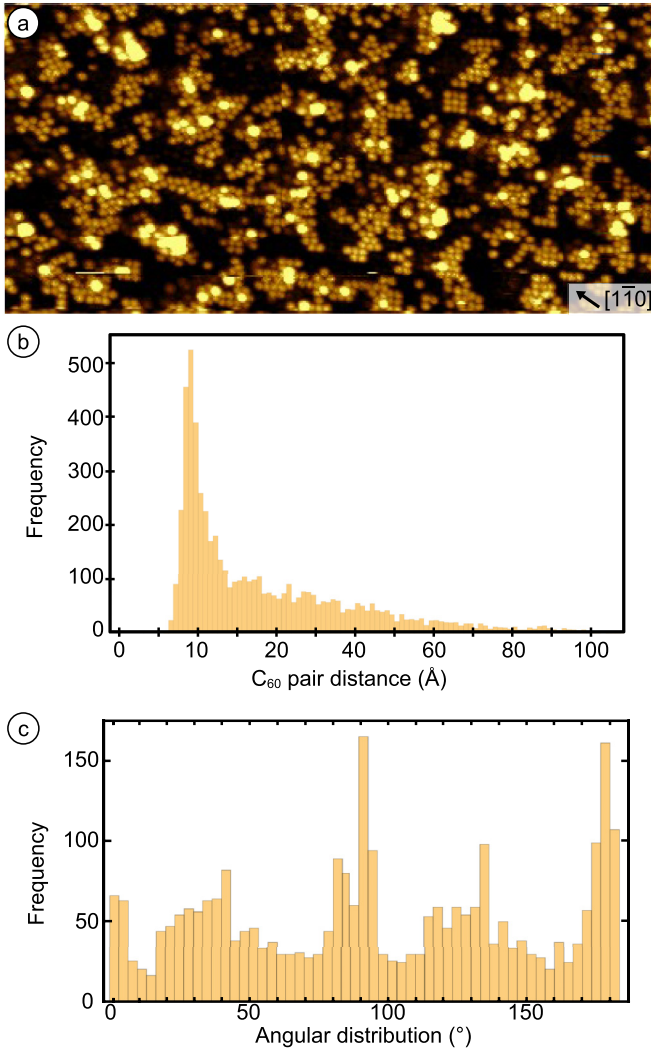


FIG. 9. (a) Large-scale STM image of 0.6 ML C_{60} deposited onto the σ -phase approximant at 150 K. (b) Radial distribution function of intermolecular distances in C_{60} pairs. (c) Orientation distribution of C_{60} pairs for distances between 7.7 and 15.3 Å. (a) $84 \times 40 \text{ nm}^2$, $\Delta z = 6 \text{ Å}$, 1 nA, 2.6 V.

one, which occurs at 0° and 90° , has been set to 9.9 Å to calibrate the STM data set. As a consequence, the second-nearest-neighbor distance corresponds to 12.8 Å, which nicely matches the grid of the template along the unit vectors of

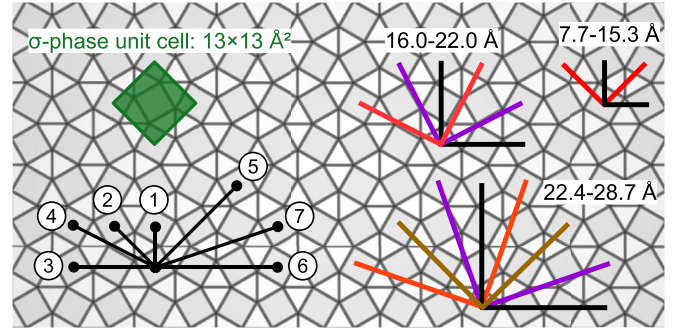


FIG. 10. Schematics illustrating the alignment of C_{60} pairs adsorbed on the σ -phase approximant.

the σ phase. The good agreement of the expected values of distances and orientations of C_{60} pairs centered above the squares with the experimentally determined ones confirms the preferential adsorption of these sites. The reason why C_{60} does not form extended or more compact patches is the mismatch of the next-neighbor distance between the squares in the template and the vdW diameter of the molecules. It results in a dephasing of the two grids after a small number of repeating units.

An alternative to adsorption in the square centers would be adsorption in the center of pairs of triangles in the σ -phase tiling. However, two different types of these pairs are present in the σ phase, which arrange in alternating sequences [18]. They differ in their atomic decoration: One pair is decorated by a central Ba atom. In the other pair, Ba atoms decorate the edges of the triangles, and the center is empty. Hence, equivalent sites centered above pairs of triangles would result in a period doubling. Thus, C_{60} adsorption on these pairs can be excluded.

With the knowledge of favored adsorption above squares, the characteristics of C_{60} adsorption on the OQC can be understood. In this template not only the loss of coherence due to the slightly different lengths scales disturbs the formation of long-range ordered patches. Additionally, the presence of a third tiling element, the rhomb, does not allow extended patches to form since the rhombs are too narrow to take up C_{60} molecules. Figure 11 illustrates the possible adsorption configurations of the C_{60} motifs shown in Figs. 6(b)–6(i). The largest compact cluster of C_{60} molecules which can be formed without crossing a rhomb consists of three triangles and two squares, as reported in Fig. 6(g). Five-membered rings

TABLE I. Ideal distance and orientations resulting from connecting neighboring squares in the σ -phase lattice according to the labeling in Fig. 10 and the experimentally obtained values from Figs. 7 and 8.

	Ideal length (Å)	Ideal orientation (deg)	Measured length (Å)	Measured orientation (deg)
1	9.4	0, 90	9.9	0, 90
2	13.0	45, 135	12.8	40, 130
3	18.4	0, 90	16.0–21.0	0, 20, 60, 90, 115, 150
4	20.6	26.6, 63.4, 116.6, 153.4		
5	26.0	45, 135		
6	27.6	0, 90	22.4–28.7	15, 40, 70, 90, 110, 130, 160, 175
7	29.1	18.4, 71.6, 108.4, 161.6		

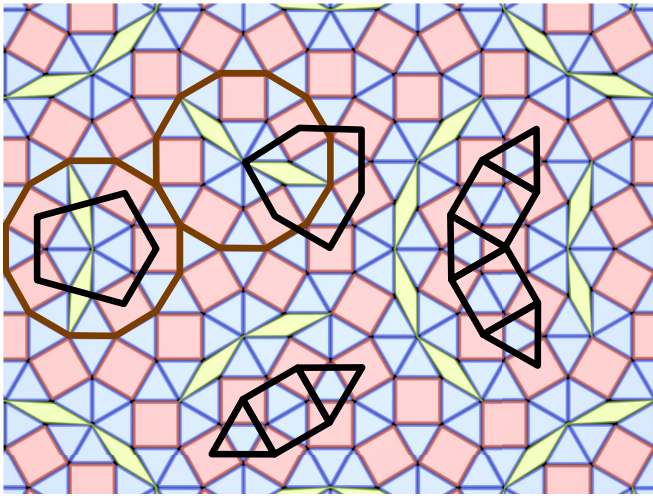


FIG. 11. Schematics of the adsorption of C₆₀ on the OQC template. The motifs observed in Figs. 6(b)–6(i) arise from connecting the centers of neighboring squares. The brown dodecagons mark the characteristic building block of the OQC.

presumably result from C₆₀ decoration of the characteristic dodecagons of the OQC (marked in brown in Fig. 11). The two larger lengths that result from bridging the distance between squares via a rhomb can also be anticipated from the STM measurement [Fig. 6(h)]. To construct a six-membered ring, as seen in Fig. 6(i), most likely a defect in the center of the dodecagon is needed because only at the rim of these dodecagons can squares in the right arrangement be found.

The room temperature STM and LEED data show that the attractive C₆₀-C₆₀ pairwise lateral interaction leads to hexagonal C₆₀ islands, as also found for many other substrates. On the other hand, the low-temperature data at low coverages indicate a site preference for the square tiling elements. This site preference is, however, weaker than the lateral C₆₀-C₆₀ interaction. Therefore, we expect hexagonal C₆₀ islands that try to maximize the occupation of square sites of the NGT. The structural optimization might lead to lateral shifts or rotations of the C₆₀ islands. To demonstrate this, we simulated the matching of C₆₀ positions within a hexagonal island with preferred square sites of the NGT under 0° and 15° rotations. The intermolecular distance of C₆₀ has been taken to be 9.9 Å following the LEED analysis. To evaluate the preferred alignment between the different grids, the number of coinciding hexagonal lattice sites with a central area of the squares has been counted. Figure 12(a) shows the principle scheme of our calculations. A central region covering 50% of the area inside the squares has been defined as the preferred adsorption site. If the hexagonal grid hits one of these sites, it is counted as a realized preferred adsorption site and is marked with a red circle. On a larger scale, the realized square tiling adsorption sites are marked (red circles) in Fig. 12(b). In total, a system of 950 squares and 1270 points of the hexagonal lattice has been evaluated. Figure 12(b) shows the combined results for 0° and 15° rotations. To be independent of the starting configuration, the hexagonal lattice has been offset versus the NGT to 46 different positions within half of the hexagonal unit cell. A maximum of 182 coincidences has

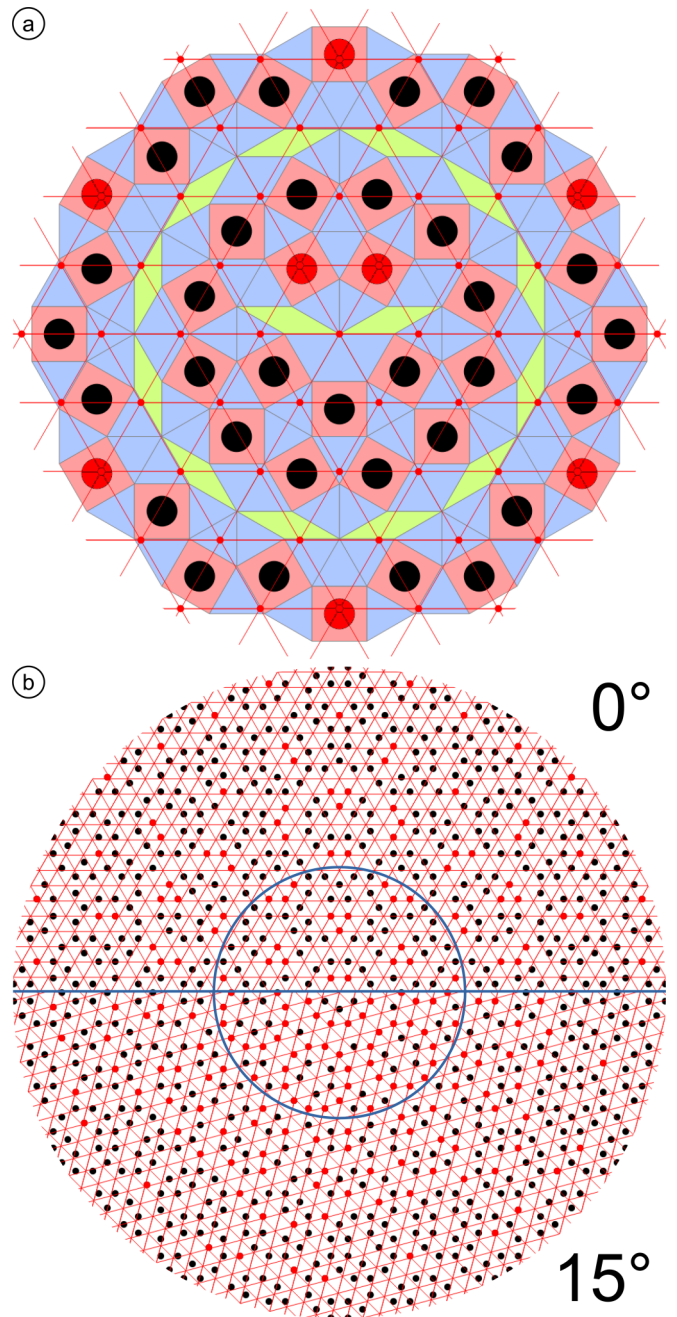


FIG. 12. (a) Superposition of the ideal dodecagonal Niizeki-Gähler tiling with an edge length of 6.85 Å and a hexagonal grid with a length of 9.9 Å. The red and black circles mark matching and nonmatching conditions, respectively. (b) Visualization of the matching condition between the hexagonal lattice and the square positions in the dodecagonal NTG for two rotational angles (0° and 15°) between the grids. For 15° rotation of the hexagonal lattice the number of coincidences is strongly increased. The difference is most pronounced in the inner part marked by the blue circle.

been found for placing the origin of the hexagonal lattice in the center of the dodecagon, as illustrated in Fig. 12(a). The number of coincidences drastically increases for a 15° rotation. There, 270 squares are hit by the hexagonal lattice in the center, which corresponds to an increase of 48%. The relative difference is more strongly enhanced when the regions inside

the blue circle in Fig. 12(b) are compared, which corresponds to the situation of small islands. Here, we count 38 hits for 0° and 90 for 15° . This corresponds to an increase of 137%. The difference in the dependence of the system size relates to the fact that for 0° rotation the coinciding points homogeneously distribute in pairs or clusters of three across the entire system. This results in a quadratic scaling with increasing diameter. However, in the case of 15° rotation a very good match is observed in the center before a dephasing of the grids sets in with increasing distance to the origin. The given system size represents almost the minimum before the matching will improve again for larger systems. Thus, a behavior analogous to a small misfit moiré pattern is observed here.

This analysis nicely explains the preferred rotation by 15° against the edges of the OQC tiling within small hexagonal C_{60} islands as observed by STM upon room temperature adsorption. It also explains why these small islands do not merge into homogeneous layers even upon annealing at temperatures slightly below the desorption temperature. A large number of islands of a limited size with a good local match will result in a lower total energy of the system compared to extended islands that only partially exhibit a good match with the template.

V. SUMMARY

In conclusion, we reported here on the formation of C_{60} clusters on the σ -phase approximant and on the OQC at 150 K. On the approximant, quadratic patches are formed, and

preferred absorption sites on the squares of the template were identified by analyzing the distances and angular distributions within pairs of C_{60} molecules. However, no extended patches are formed because of the mismatch between the vdW diameter of the molecules and the grid provided by the squares of the periodic template, which causes the loss of coherence after a few repeating units. C_{60} adsorption studies on the OQC at low temperatures confirm the center of the squares is the preferred adsorption site. The molecules adopt the grid of the dodecagonal template in small clusters consisting mainly of triangles and squares. The presence of rhombs in this tiling was found to prevent the formation of larger patches. In addition, the formation of hcp patches was observed that are in registry with the template. The interaction of the C_{60} molecules with the two-dimensional oxide film is generally weak, as expressed by a low desorption temperature of 510 K. At room temperature hexagonally ordered islands are formed that show a slightly preferred orientation of 15° with respect to the tiling edges. Under this rotational angle a maximum of C_{60} molecules in the hexagonal grid is centered about the squares of the OQC.

ACKNOWLEDGMENTS

This work is supported by the Deutsche Forschungsgemeinschaft through the collaborative research center SFB 762 (Functionality of oxidic interfaces, projects A3 and B8). We thank R. Kulla for technical support.

-
- [1] D. Shechtman, I. Blech, D. Gratias, and J. W. Cahn, *Phys. Rev. Lett.* **53**, 1951 (1984).
 - [2] H. R. Sharma, M. Shimoda, and A. P. Tsai, *Adv. Phys.* **56**, 403 (2007).
 - [3] J. Ledieu, L. Leung, L. H. Wearing, R. McGrath, T. A. Lograsso, D. Wu, and V. Fournée, *Phys. Rev. B* **77**, 073409 (2008).
 - [4] K. J. Franke, H. R. Sharma, W. Theis, P. Gille, Ph. Ebert, and K. H. Rieder, *Phys. Rev. Lett.* **89**, 156104 (2002).
 - [5] V. Fournée and P. A. Thiel, *J. Phys. D* **38**, R83 (2005).
 - [6] H. R. Sharma, J. A. Smerdon, P. J. Nugent, A. Ribeiro, I. McLeod, V. R. Dhanak, M. Shimoda, A. P. Tsai, and R. McGrath, *J. Chem. Phys.* **140**, 174710 (2014).
 - [7] N. Kalashnyk, J. Ledieu, É. Gaudry, C. Cui, A.-P. Tsai, and V. Fournée, *Nano Res.* **11**, 2129 (2018).
 - [8] H. R. Sharma, J. A. Smerdon, K. M. Young, and R. McGrath, *J. Phys.: Condens. Matter* **24**, 354012 (2012).
 - [9] K. M. Young, J. A. Smerdon, H. R. Sharma, M. Lahti, K. Pussi, and R. McGrath, *Phys. Rev. B* **87**, 085407 (2013).
 - [10] J. Ledieu, C. A. Muryn, G. Thornton, R. D. Diehl, T. A. Lograsso, D. W. Delaney, and R. McGrath, *Surf. Sci.* **472**, 89 (2001).
 - [11] J. Ledieu, É. Gaudry, V. Fournée, J. A. Smerdon, and R. D. Diehl, *Z. Kristallogr.* **232**, 629 (2017).
 - [12] J. A. Smerdon, K. M. Young, M. Lowe, S. S. Hars, T. P. Yadav, D. Hesp, V. R. Dhanak, A. P. Tsai, H. R. Sharma, and R. McGrath, *Nano Lett.* **14**, 1184 (2014).
 - [13] V. Fournée, É. Gaudry, J. Ledieu, M.-C. de Weerd, D. Wu, and T. Lograsso, *ACS Nano* **8**, 3646 (2014).
 - [14] J. Ledieu, É. Gaudry, V. Fournée, *Sci. Technol. Adv. Mater.* **15**, 034802 (2014).
 - [15] M. Paßens, V. Caciuc, N. Atodiresei, M. Feuerbacher, M. Moors, R. E. Dunin-Borkowski, S. Blügel, R. Waser, and S. Karthäuser, *Nat. Commun.* **8**, 15367 (2017).
 - [16] S. Förster, K. Meinel, R. Hammer, M. Trautmann, and W. Widdra, *Nature (London)* **502**, 215 (2013).
 - [17] S. Schenk, S. Förster, K. Meinel, R. Hammer, B. Leibundgut, M. Paleschke, J. Pantzer, C. Dresler, F. O. Schumann, and W. Widdra, *J. Phys.: Condens. Matter* **29**, 134002 (2017).
 - [18] S. Förster, M. Trautmann, S. Roy, W. A. Adeagbo, E. M. Zollner, R. Hammer, F. O. Schumann, K. Meinel, S. K. Nayak, K. Mohseni, W. Hergert, H. L. Meyerheim, and W. Widdra, *Phys. Rev. Lett.* **117**, 095501 (2016).
 - [19] N. Niizeki and H. Mitani, *J. Phys. A* **20**, L405 (1987).
 - [20] F. Gähler, in *Quasicrystalline Materials: Proceedings of the ILL/CODEST Workshop* (World Scientific, Singapore, 1988), p. 13.
 - [21] S. Schenk, E. M. Zollner, O. Krahn, B. Schreck, R. Hammer, S. Förster, and W. Widdra, *Acta Crystallogr., Sect. A* **75**, 307 (2019).
 - [22] M. Hohage, T. Michely, and G. Comsa, *Surf. Sci.* **337**, 249 (1995).
 - [23] D. Nečas and P. Klapetek, *Cent. Eur. J. Phys.* **10**, 181 (2012).